Theoretical investigation on correlating time-of-flight 3D sensation error

Lu Chunqing, Song Yuzhi, Wu Yanpeng, Yang Mengfei

(China Academy of Space Technology, Beijing 100081, China)

Abstract: Time-of-flight measurement is one of the principles of 3D sensation systems. In recent years, with the development of semiconductor technology, time-of-flight measurement systems based on the signal correlation method have developed rapidly in the field of three-dimensional imaging due to its advantages of all solid-state components, high integration and low power consumption. The mathematical principles of correlation time-of-flight measurement techniques were systematically studied, its error sources were analysed, the mathematical models were constructed, and different types of measurement errors were compared. The research results show that light source error, multipath and ambient light interference are the main factors that restrict the measurement accuracy and application range of time-of-flight imaging systems.

Key words: 3D sensation; time-of-flight; correlation function; active imaging; anti-saturation

CLC number: TP212.14 **Document code**: A **DOI**: 10.3788/IRLA201948.1113002

基于相关法飞行时间三维感知的误差机理研究

卢纯青,宋玉志,武延鹏,杨孟飞

(中国空间技术研究院,北京 100081)

摘 要:飞行时间测量是三维感知系统的重要原理之一。近年来随着半导体技术的发展,基于信号相关法的飞行时间测量系统以其无活动部件、高集成度、低功耗的优势,在三维成像领域迅速发展。文中系统研究了基于信号相关的飞行时间测量技术的数学原理,分析了其误差来源及其数学模型,并进行了横向对比。研究结果表明:飞行时间成像系统的光源误差、多路径误差和环境光是制约测量精度和适用范围的主要因素。

关键词:三维感知; 飞行时间; 相关函数; 主动式成像; 抗饱和

收稿日期:2019-09-05; **修订日期**:2019-10-15

作者简介:卢纯青(1988-),男,工程师,主要从事空间成像感知与智能导航控制技术方面的研究。Email:cust0702@sina.com

0 Introduction

Many principles have been proposed for 3D measurement techniques by optical means. The major categories are time-of-flight measurement, triangulation methods and shape-from-shading. This paper discusses the correlating time-of-flight imaging theory and measurement errors and builds a prototype based on time-of-flight imaging measurements to verify the measurement error unique to TOF imaging. The conclusion shows that the source error, brightness-related error and ambient light of the time-of-flight imaging system are the main factors that restrict the measurement accuracy and application range.

1 Theory of correlating TOF

Correlating TOF ranging measures the distance from the sensor pixel to the scene by calculating the phase shift of the optical signal propagating in space according to the signal correlation theory; thus, the method is an indirect measurement method. The principle is that the light source emits a pulsed or a modulated light signal to the scene, and the detector receives the reflected light signal; it then obtains a phase change of the reflected light signal from a correlation function between the signal and the reference signal (light source driving signal) and calculates the phase shift of the reference signal. The time of flight of the signal obtains in turn the depth information between the measured scene and the focal plane of the sensor.

Let the light source modulation function be a periodic function $O(f_m,t)$ with the frequency f_m. Since the modulation frequency is a constant during light propagation, the optical signal collected by the sensor is $I(f_m,t)$. Then, in the correlation function, the phase shift α_n can be calculated by the following cross-correlation function[1-2]

$$I_n(f_m,\alpha_n)=\frac{1}{t_1'-t_0'}\int_{t_2'}^{t_1'}I(f_m,t+t_d)\cdot O\left(f_m,t+\frac{\alpha_n}{2\pi f_m}\right)\mathrm{d}t=\frac{1}{t_1-t_0}\cdot\int_{t_0}^{t_1}I(f_m,t)\cdot O\left(f_m,t+\frac{\alpha_n}{2\pi f_m}+t_d\right)\mathrm{d}t \tag{1}$$

where t_0 and t_0' are the moments when the sensor starts to integrate, and t_1 and t_1' are the moments when the sensor ends the integration; then t_1-t_0 and $t_1'-t_0'$ are the integration times of the sensor. Expand $O(f_m,t)$ and $I(f_m,t)$ into Fourier series, then

$$O(f_m,t)=\sum_{j=-\infty}^{\infty}O_j\mathrm{e}^{ijwt} \tag{2}$$

$$I(f_m,t)=\sum_{k=-\infty}^{\infty}I_k\mathrm{e}^{ikwt} \tag{3}$$

where ω is the modulation angular frequency of the light source

$$\omega=2\pi f_m \tag{4}$$

Substituting the function in the form of a Fourier series into the above formula and further simplifying,

$$\mathrm{In}(f_m,\alpha_n)=I_0O_0+\frac{I_1O_1}{2}(\cos(\Phi_0)\cos(\Phi_0+\alpha_n+\omega t_d))+\sin(\Phi_0)\sin(\Phi_0+\alpha_n+\omega t_d) \tag{5}$$

This formula has the form of a trigonometric function, which denotes I_0O_0 as c, $I_1O_1/2$ as A, and ωt_d as φ_d, which can be further simplified as

$$I_n(f_m,\alpha_n)=c+A\cdot\cos(\alpha_n+\varphi_d)=c+\frac{A}{2}(\mathrm{e}^{-2\pi i\frac{n}{N}}\mathrm{e}^{-i\varphi_d})+\frac{A}{2}(\mathrm{e}^{2\pi i\frac{n}{N}}\mathrm{e}^{i\varphi_d}) \tag{6}$$

Write the form of the linear matrix equation

$$\begin{pmatrix}1 & 1 & 1\\ u^1 & \bar{u}^1 & 1\\ \vdots & \vdots & \vdots\\ u^{N-1} & \bar{u}^{N-1} & 1\end{pmatrix}\cdot\begin{pmatrix}\frac{A}{2}z\\ \frac{A}{2}\bar{z}\\ c\end{pmatrix}=\begin{pmatrix}I_0\\ \vdots\\ I_{N-1}\end{pmatrix} \tag{7}$$

where $u=\mathrm{e}^{\frac{2\pi i}{N}}$, $z=\mathrm{e}^{i\varphi_d}$, and the matrix equation above can be simplified as

$$M_{N\times3}\cdot P_{3\times1}=d_{3\times1} \tag{8}$$

To make the matrix P have a unique solution, $N\geqslant3$ is needed. When $N=3$, the equation has a unique solution; when $N>3$, the equation has a least squares solution. That is, the sensor collects a number N of reflected light signals for not fewer than 3 times to restore the parameters of the original signal. The

least squares solution of the matrix P_{sol} is

$$P_{sol}=(M^{*}M)^{-1}M^{*}\cdot d=\frac{1}{N}M^{*}d \tag{9}$$

The above formula is a unique solution (generally N=4); in practical applications when N=3, the equations have a least-squares solution

$$c=\frac{1}{4}\sum_{n=0}^{3}I_n \tag{10}$$

$$A=\frac{1}{2}|I_0-I_2+i(I_3-I_1)| \tag{11}$$

$$\varphi_d=\arctan\frac{I_3-I_1}{I_2-I_0} \tag{12}$$

The distance Z is then

$$Z=\frac{c\cdot\varphi_d}{4\pi f_m}=\frac{c}{4\pi f_m}\cdot\arctan\frac{I_3-I_1}{I_2-I_0} \tag{13}$$

2 Error analysis

2.1 Statistical error

The statistical noise of the time-of-flight imaging device includes shot noise, dark current, trap noise, reset noise, and 1/f noise, where the main noise component is the photon′s shot noise. In engineering applications, the signal-to-noise ratio (SNR) and dynamic range (DR) are generally used to characterize the noise performance of the imaging device. The signal-to-noise ratio expression is as follows[3]

$$SNR=20\log\left(\frac{\Delta U_{signal}}{\Delta U_{noise}}\right) \tag{14}$$

where ΔU_{signal} is the output voltage swing and ΔU_{noise} is the rms noise of the output voltage. The dynamic range is the ratio of the maximum swing to the dark current of the output voltage. The expression is

$$DR=20\log\left(\frac{\Delta U_{max}}{\Delta U_{DN}}\right) \tag{15}$$

In engineering applications, the dynamic range is the maximum value of the signal-to-noise ratio, i.e.,

$$DR=20\log\left(\frac{\Delta U_{max}}{\Delta U_{noise}}\right) \tag{16}$$

Regardless of the noise introduced by the readout circuit, the dynamic range of the time-of-flight imaging device can be estimated by the following equation

$$DR=20\log(\sqrt{N_{photo}})=20\log\sqrt{\frac{\Delta U_{max}C_{int}}{q}} \tag{17}$$

where N_{photo} is the maximum number of charges that can be collected by the pixel circuit equivalent capacitance C_{int}. As seen from the above equation, expanding the swing or equivalent capacitance of the voltage signal in the device design can increase the dynamic range of the pixel, and the swing of the voltage signal is generally 1–3 V.

2.2 Wiggling error

The reference signal is typically the drive signal of the light source and correlated with the electrical signal in the pixel circuit. The wiggling error is a function of the measured distance. As the measured distance increases, the measured value periodically changes around the ground truth. The main cause of such errors is the difference between the reference signal of the continuously modulated source and the ideal sinusoidal signal, which is essentially the difference between the ideal correlation function and the actual correlation function. The higher harmonics in the reference signal of the modulated light source undergo a correlation operation, causing the error of the measured value to periodically change around the true value, and the period of change depends on the intensity and frequency of the higher harmonic.

According to the formula of the phase shift and the correlation function

$$\varphi_d=\arctan\frac{I_3-I_1}{I_2-I_0} \tag{18}$$

When the reference signals are an ideal sine function and a sinusoidal function of superimposed high-frequency components, the expressions of the phase shift are

$$\varphi_d=\arctan\left(\frac{I_3^{T}-I_1^{T}}{I_2^{T}-I_0^{T}}\right)=\arctan\left(\frac{I_3^{R}-I_1^{R}}{I_2^{R}-I_0^{R}}\right) \tag{19}$$

where I_n^{T} is the correlation function of the fundamental frequency, and I_n^{R} is the correlation function superimposed with high frequency components. The above equation is established when one of the following two types of constraints is satisfied:

(1) Constraint 1: When the ideal correlation

function of the sampling phase is equal to the actual correlation function,

$$I_n^R = I_n^T \ \forall\ n \in \{0,1,2,3\} \tag{20}$$

(2) Constraint 2: The error between the ideal correlation function and the measurement correlation function is denoted as δI_n^R, defined as

$$\delta I_n^R = I_n^R - I_n^T \ \forall\ n \in 0,1,2,3 \tag{21}$$

$$\varphi_d = \arctan\left(\frac{a+\delta a}{b+\delta b}\right) \tag{22}$$

with $a = I_3^T - I_1^T$, $b = I_2^T - I_0^T$, $\delta a = I_3^R - I_1^R$, $\delta b = I_2^R - I_0^R$. When

$$\frac{a}{b} = \frac{\delta a}{\delta b} \tag{23}$$

the equation is established.

The impact on distance calculations is shown in Fig.1. The plot shows two signals with higher Fourier modes, and the resulting depth is compared to ground truth when correlating each of these functions with themselves. The depth can then be calculated from the results using the equations which implicitly rely on sinusoidal shaped signals. Even harmonics do not introduce an error in the depth calculation, as seen in the two plots on the left. Only even harmonics were used here, and the lower plot shows that no systematic error is introduced. The plots on the right side are created using a function with odd harmonics. The lower plot shows significant errors in the depth calculation-the measured depth wiggles around the ground truth. However, it also shows that if the higher modes are sufficiently suppressed-as is the case in all TOF −systems, and in this example, the bijective nature between calculated depth and real depth is not broken.

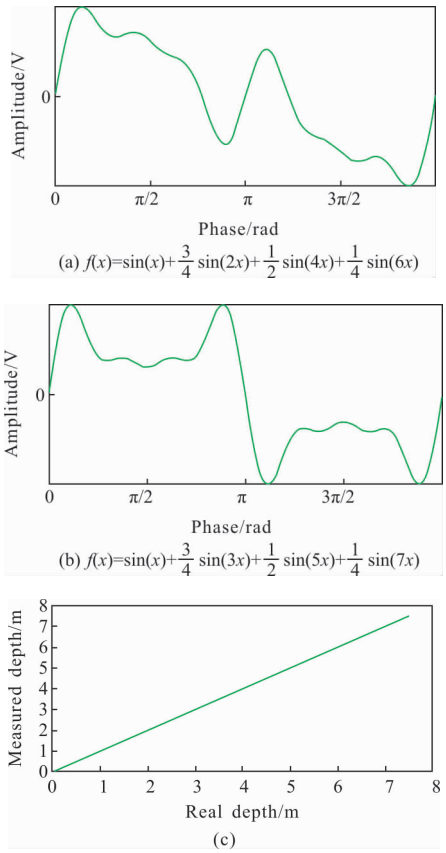

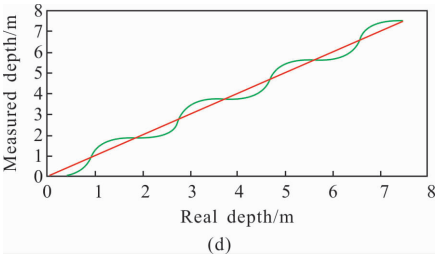

Fig.1 Signal forms (a), (b) and resulting depth (c), (d) after autocorrelation compared to correct depth for the two correlation functions with higher Fourier modes

Table 1 shows a summary of all the different effects investigated and how much they impact the data of the camera systems. The wiggling error is the dominating effect for all three cameras, but its total amount varies very much between the systems. The O3D shows the strongest deviation. The second strongest effect is the integration time offset. The 19 k shows a very good behaviour here, while for the SR−3000 this effect is nearly as big as the wiggling error. The pixel offset is quite similar for all camera types, and the static effects have the smallest impact of all variables.

Tab.1 Overview of the total amount of the depth error of different effects

Error	19 k	SR−3000	O3D
Wiggling error/mm	80	120	200
Integration time offset/mm	35	100	60
Pixel offset/mm	20	20	20
Statistical error/mm	±23	±9	±9

The correction of the wiggling error includes a method of increasing the number of sampling[4], a method of calibrating the residual of the measurement result [5-6], and a method of phase-modulating the amplitude signal[7-8]. The method of increasing the number of samplings theoretically extends the Eq.(7), so the dimension of the phase solving matrix is increased, and the signal recovery accuracy is improved; the residual calibration sets the wiggling error to a fixed mode error, and the measurement result using an external measuring instrument is used. The measurement results are calibrated to form a residual distribution matrix to eliminate measurement errors. The essence of the phase modulation method is to solve the problem of insufficient sampling rate by phase encoding.

2.3 Amplitude-related error

The amplitude error is a function of the amplitude of the reflected light signal, depending on the intensity of the reflected light received by the sensor. Thus, the lower the reflectivity of the object, the smaller the amplitude of the optical signal received by the sensor and the greater the error of the measurement result of the distance. Abbreviating the above formula as a map between correlation functions and signal parameters gives[2]:

$$I=[I_1I_2I_3I_4] \tag{24}$$

$$S=(A,\varphi_d,c)^{\mathrm{T}} \tag{25}$$

$$S=f(I) \tag{26}$$

$$f:R^4\rightarrow R^+\times[0,2\pi]\times R \tag{27}$$

with

$$f_1=\begin{pmatrix} \frac{1}{2} & 0 & -\frac{1}{2} & 0 \\ 0 & -\frac{1}{2} & 0 & \frac{1}{2} \\ \frac{1}{4} & \frac{1}{4} & \frac{1}{4} & \frac{1}{4} \end{pmatrix} \tag{28}$$

$$f_2(A,\varphi_d,c)=(\Phi^{-1}(A,\varphi_d),c) \tag{29}$$

Now, assume the simple special case in which the measurements of the I′s are i.i.d, in this case,

$$\mathrm{Var}(A,\varphi_d,c)=Df(\mu)\mathrm{Var}(I)Df(\mu)^{\mathrm{T}}=Df(\mu)Df(\mu)^{\mathrm{T}}\sigma^2=$$

$$\mathrm{diag}\left(\frac{1}{2},\frac{1}{2A^2},\frac{1}{2}\right)\sigma^2 \tag{30}$$

2.4 Multipath

Multipath error refers to an error caused by phase aliasing due to scattering of optical signal. This kind of error appears in the following four physical scenarios:

(1) When the solid angle of the sensor pixel covers the boundary of the foreground and the background in the scene, the collected optical signal comes from the superposition of the reflected light of the pixel field of view, and the measurement result is within the interval of the foreground depth and the background depth (the middle value). The reason for such errors under this condition is due to the limited spatial resolution of the time-of-flight sensor, so when the scene depth gradient in the pixel field of view is greater than the spatial resolution of the sensor, the pixels receive different phase differences. Reflecting the optical signal, phase aliasing occurs at the pixel, resulting in an error in the measured value.

(2) When the imaging surface of the sensor does not coincide with the ideal image plane of the optical system, the scene area covered by the pixel scene is enlarged, and the spatial resolution of the imaging system is decreased. If the gradient of the scene depth is greater than the spatial resolution, the sensor pixel receives phase aliasing in the optical signal, and the measured value error increases.

(3) The suspended particles in the light propagation medium cause the optical signal to scatter on the transmission path. Some of the optical signals are reflected into the sensor before they reach the surface of the scene, so the measurement data with error appears in the ranging results.

(4) In reality, only a portion of the optical signal received by the optical system enters the potential well in the sensor pixel circuit, and another portion of the optical signal is scattered multiple times on the optical system component and the sensor surface. Therefore, the modulation phase of the optical signal received by the pixel is a superposition of the above signals, forming a phase alias.

In summary, multipath effects are common in the physical process of time-of-flight imaging. The sources of multipath are shown in Fig.2.

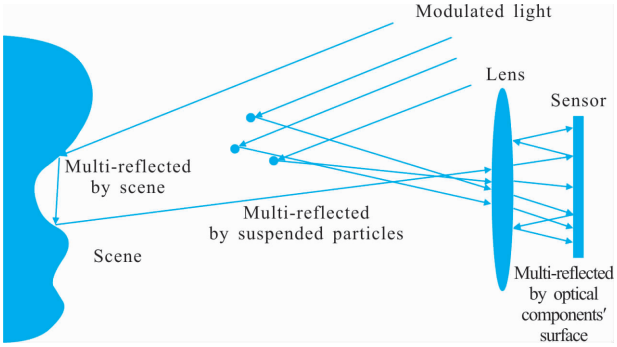

Fig.2 Schematic diagram of multipath effects in reality

By the aperture imaging model, the pixel has a corresponding relationship with an area in the scene through the optical system. The reflected light of the area 1 is η_1, and the reflected light of the area 2 is η_2[14-15]

$$\eta_1=A_1e^{i\varphi_{d_1}} \tag{31}$$

$$\eta_2=A_2e^{i\varphi_{d_2}} \tag{32}$$

The reflected light signals passing through the two regions pass through the optical system to the same sensor pixel S_0, and the received optical signal is

$$\xi=\eta_1+\eta_2=A_1e^{i\varphi_{d_1}}+A_2e^{i\varphi_{d_2}} \tag{33}$$

The amplitude and phase of the superimposed light vector are

$$A=\sqrt{A_1^2+A_2^2+2A_1A_2\cos(\varphi_{d_1}+\varphi_{d_2})} \tag{34}$$

$$\varphi_d=\arctan\frac{A_2\sin(\varphi_{d_1}+\varphi_{d_2})}{A_1+A_2\cos(\varphi_{d_1}+\varphi_{d_2})} \tag{35}$$

with

$$\varphi_{d_2}>\varphi_{d_1}>0 \tag{36}$$

$$\varphi_{d_1}<\varphi_d<\varphi_{d_2} \tag{37}$$

In practical applications, the modulated light will be received by the sensor after multiple reflections from mentioned source above; this results in the actual propagation path of the optical signal being larger than the theoretical propagation path and the optical signal passing through different propagation paths in the pixel. Superimposed on each other, this causes an error between the measured depth and the theoretical depth. In the time-of-flight imaging system, the sensor S and the light source L are included, and a pixel S_0 of the sensor S covers the area ΔP of the image centred on the P point in the scene. Then, the light signal emitted by the light source L is reflected by the P point in the scene. The propagation path to the cell S_0 is

$$L_L\rightarrow P\rightarrow S \tag{38}$$

Since the light signal of the light source L is full field illumination, when the light signal is irradiated to another point P' in the scene, the portion is reflected by the P' point since the reflective property of the material surface follows a cosine distribution or a bidirectional reflection function. The optical signal will continue to illuminate to point P. After the second reflection of point P, it will reach the pixel S_0, and the propagation path is

$$L_L\rightarrow P'\rightarrow P\rightarrow S \tag{39}$$

Set the modulated optical signal as

$$\eta=Ae^{i\varphi_d} \tag{40}$$

The received optical signal is a superposition of optical signals reflected by the points in the scene to the field of view of the pixel

$$\xi=\sum_{n=1}^{N}\eta_n=A_1e^{i\varphi_{d_1}}+\sum_{n=1}^{M}A_{n-1}e^{i\varphi_{d_{n-1}}} \tag{41}$$

where $A_1e^{i\varphi_{d_1}}$ is the light signal reflected once by the scene and is the vector of the reflected light signal received by the pixel. $\sum_{n=1}^{M}A_{n-1}e^{i\varphi_{d_{n-1}}}$ is the reflected light signal of other bins in the scene field of the pixel.

The method of identifying and correcting the flying pixels is still in development, and the correction effect is not satisfactory. The methods for identifying the flying pixels in depth data is based on the confidence-based method proposed by Reynolds et al[16]. For the flying pixels correcting methods, there are currently the median filtering method proposed by Hebert and Krotov and the multi-sensor based method proposed by Cui[17]. The flying pixel correction method, but when the phase difference is less than π, the median filtering appears to remove the correct data,

and the method proposed by Schuon requires multiple sensors to acquire sub-pixel accuracy measurement data for the same scene. Marco [18] et al use deep neutral network to eliminate flying pixels resulting from the scene structure.

2.5 Ambient light

Ambient light interference means that the scene is simultaneously illuminated by the light source of the time-of-flight imaging system and other light sources (such as the sun and indoor lighting); this makes the average optical power entering the pixel too large, resulting in an increase or even error in the error of the measured data. The mathematical model of the background optical signal is a constant value; the modulated optical signal periodically changes, and they are linearly superimposed. Since the sensor pixel collects the photo-generated charge in the well, the amount of charge that can be collected has a limit, which is called the full-trap charge. When the potential wells for the correlated acquisition of the optical signal reach the full well, the pixel circuit cannot reflect the correlation between the value of the reference voltage and the amount of charge between the potential wells, resulting in an error in the measurement result. Mathematically, there is a non-linear relationship between the optical signal and the amount of charge. If there is no ambient light signal, the modulation contrast of the pixel is defined as

$$K_{\mathrm{PMD}}=\frac{\Delta U_{\max}-\Delta U_{\min}}{\Delta U_{\max}+\Delta U_{\min}} \tag{42}$$

If there is an ambient light signal, the modulation contrast is

$$K=\frac{K_{\mathrm{PMD}}}{1+\dfrac{P_{\mathrm{background}}}{P_{\mathrm{opt}}}} \tag{43}$$

where P_{opt} is the optical power of the modulated light source and $P_{\mathrm{background}}$ is the optical power of the ambient light signal. When ambient light is present, the modulation contrast of the optical signal is attenuated. In terms of ambient light suppression, it is mainly realized by optimizing the pixel circuit structure[19-21].

Figures 3 and 4 show the results of a time-of-flight imaging system imaging a scene without ambient light or ambient light, respectively. The optical power of the ambient light source is one solar constant. It can be seen from the comparison that in the illumination of ambient light, the diffuse reflector in the central region of the image is saturated due to the optical signal, resulting in a measurement result of 0 in this region.

Fig.3 Imaging results without ambient light illumination

Fig.4 Imaging results of 1 solar constant ambient light illumination

3 Conclusions

According to the theoretical analysis and experimental results of the time-of-flight imaging error source, it can be seen that statistical error and light source wiggling error are internal errors of the imaging system, and the mathematical model is accurate, so it can be removed using a specific correcting model. Amplitude-related error associates with the power of the light source and the reflectivity of the scene. This type of error can be reduced by increasing the power of the system light source. Multipath error and ambient error are coupled with the scene structure and the optical transmission medium, so it leads to largest data error, which is difficult to

correct. The error range and correction difficulty of the above five types of error are shown in Tab.2.

Tab.2 Comparison of TOF error modes

Error	Scale	Correction difficulty
Statistical error	mm	Easy
Wiggling error	mm	Medium
Amplitude-related error	cm	Medium
Multipath	mm to m	Hard
Ambient light	no data	Hard

This paper discusses a general conspectus about correlating time-of-flight ranging model and measurement error. A theoretical model was presented and verified with three kinds of 3D-TOF ranging systems, five types of TOF measurement error is compared. From all types of error above, the limitations of current TOF systems are light source, multipath and ambient light. Respectively, the influence of light source appears as wiggling error, it results from the influence of the higher harmonics of the modulated light source signal on the phase sampling. For multipath effect, measurement result appears as flying pixels which is universal in TOF model, that is, the phase aliasing of modulated optical signals on multiple propagation paths in a pixel. For ambient light, it depends on the condition of application, which leads to the ranging data down to 0. Furthermore, TOF systems work well in absolute darkness. While artificial light doesn′t pose a substantial problem for current systems since it does not contain any mentionable IR fraction, ambient light is the strict contrary: it contains a high IR fraction and disturbs the measurements because it effectively reduces the amplitude by increasing the constant DC offset.

References:

[1] Lange R. 3D time-of-flight distance measurement with custom solid-state image sensors in CMOS/CCD-technology [D]. Siegen: University of Siegen, 2000.

[2] Plaue M. Technical report: analysis of the PMD imaging system[D]. Heidelberg: University of Heidelberg, 2006.

[3] Falie D, Buzuloiu V. Noise characteristics of 3D time-of-flight cameras[C]//2007 International Symposium on Signals, Circuits and Systems. IEEE, 2007, 1: 1-4.

[4] Lee C, Kim S Y, Choi B, et al. Depth error compensation for camera fusion system [J]. ***Optical Engineering***, 2013, 52 (7): 073103.

[5] Schmidt M, Jähne B. A physical model of time-of-flight 3D imaging systems, including suppression of ambient light[C]// Workshop on Dynamic 3D Imaging, 2009: 1-15.

[6] Dorrington A A, Cree M J, Carnegie D A, et al. Video-rate or high-precision: A flexible range imaging camera [C]// SPIE, 6813: 681307.

[7] Fuchs S, May S. Calibration and registration for precise surface reconstruction with time-of-flight cameras [J]. ***International Journal of Intelligent Systems Technologies and Applications***, 2008, 5(3-4): 274-284.

[8] Lindner M, Kolb A. Lateral and depth calibration of PMD-distance sensors [C]//International Symposium on Visual Computing, 2006: 524-533.

[9] Fersch T, Weigel R, Koelpin A. A CDMA modulation technique for automotive time-of-flight LiDAR systems [J]. ***IEEE Sensors Journal***, 2017, 17(11): 3507-3516.

[10] Ai X, Nock R, Rarity J G, et al. High-resolution random-modulation cw lidar [J]. ***Applied Optics***, 2011, 50 (22): 4478-4488.

[11] Atalar O, Van Laer R, Sarabalis C J, et al. Time-of-flight imaging system on resonant photoelastic modulation [J]. ***Applied Optics***, 2019, 58(9): 2235-2247.

[12] Gupta M, Nayar S, Velten A, et al. A geometric perspective on time-of-flight camera design [C]//SPIE, 2019, 10889: 1088902.

[13] Jongenelen A P P, Bailey D G, Payne A D, et al. Analysis of errors in tof range imaging with dual-frequency modulation [J]. ***IEEE Transactions on Instrumentation and Measurement***, 2011, 60(5): 1861-1868.

[14] Jimenez D, Pizarro D, Mazo M, et al. Modelling and correction of multipath interference in time of flight cameras [J]. ***Image & Vision Computing***, 2014, 32(1):1-13.

[15] Karel W, Ghuffar S, Pfeifer N. Quantifying the distortion of distance observations caused by scattering in time-of-flight range cameras[J]. ***International Archives of Photogrammetry***, 2010, 38 (5): 316-321.

[16] Reynolds M, Dobos J, Peel L, et al. Capturing time-of-flight

data with confidence [C]//IEEE Conference on Computer Vision and Pattern Recognition (CVPR), 2011:945-952.

[17] Cui Y, Schuon S, Chan D, et al. 3D shape scanning with a time-of-flight camera [C]//IEEE Computer Society Conference on Computer Vision and Pattern Recognition. IEEE, 2010: 1173-1180.

[18] Marco J, Hernandez Q, Munoz A, et al. DeepToF: off-the-shelf real-time correction of multipath interference in time-of-flight imaging[J]. ***ACM Transactions on Graphics* (*ToG*)**, 2017, 36(6): 219.

[19] Zach G, Davidovic M, Zimmermann H. A 16×16 pixel distance sensor with in-pixel circuitry that tolerates 150 klx of ambient light [J]. ***IEEE J Solid-State Circuits***, 2010, 45 (7): 1345-1353.

[20] Zach G, Zimmermann H. A 2×32 range-finding sensor array with pixel-inherent suppression of ambient light up to 120klx [C]//2009 IEEE International Solid-State Circuits Conference-Digest of Technical Papers, IEEE, 2009: 352-353.

[21] Sawada T, Kawahito S, Nakayama M, et al. A TOF range image sensor with an ambient light charge drain and small duty-cycle light pulse [C]//International Image Sensor Workshop, 2007: 254-257.